Trends in Surface Oxygen Formation Energy in Perovskite Oxides

Yoyo Hinuma,* Shinya Mine, Takashi Toyao, and Ken-ichi Shimizu

Cite This: *ACS Omega* 2022, 7, 18427−18433

Read Online

ACCESS | Metrics & More | Article Recommendations | SI Supporting Information

ABSTRACT: Perovskite oxides comprise an important class of materials, and some of their applications depend on the surface reactivity characteristics. We calculated, using density functional theory, the surface O vacancy formation energy (E_{Ovac}) for perovskite-structure oxides, with a transition metal (Ti−Fe) as the B-site cation, to estimate the catalytic reactivity of perovskite oxides. The E_{Ovac} value correlated well with the band gap and bulk formation energy, which is a trend also found in other oxides. A low E_{Ovac} value, which is expected to result in higher catalytic activity via the Mars−van Krevelen mechanism, was found in metallic perovskites such as $CaCoO_3$, $BaFeO_3$, and $SrFeO_3$. On the other hand, titanates had high E_{Ovac} values, typically exceeding 4 eV/atom, suggesting that these materials are less reactive when O vacancy formation is involved in the reaction mechanism.
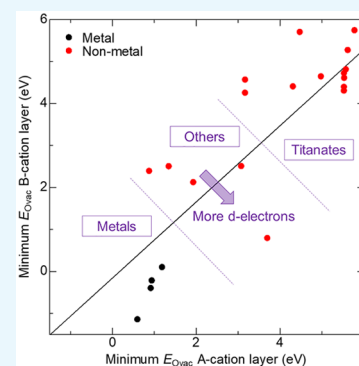
1. INTRODUCTION

Defects can significantly influence the properties of metal oxides. The most representative defect is the O vacancy,[1−3] which can strongly affect the electrical, optical, magnetic, mechanical, and catalytic properties on intentional or unintentional introduction into the metal oxide structure.[4−6] O vacancies on the surface of metal oxide catalysts often act as reaction sites for heterogeneous catalysis;[2,7] thus, the formation energy of an O vacancy at the surface (denoted as E_{Ovac} in this paper) is often used as a descriptor of the catalytic activity of metal oxides.[8]

Experimental investigations of O vacancies are difficult, although research on O vacancies in the field of catalysis is obviously important.[9] Surface O vacancies also play an important role in polaron formation and stabilization in oxides such as CeO_2[10] and TiO_2.[11] Determination of the E_{Ovac} value requires highly sophisticated techniques, and its evaluation is not always possible.[12] On the other hand, there are recent theoretical studies on the formation of O vacancies in metal oxides,[4,13] but still the number of investigated surfaces remains limited. Therefore, studies on the physical principles determining E_{Ovac} and the development of guidelines to estimate E_{Ovac} using other properties that are much easier to obtain are highly desirable.

Perovskite structure oxides make up an important class of materials.[14,15] Applications to catalysis include ethane dehydrogenation by $La_{0.8}Ba_{0.2}MnO_{3-\delta}$,[16] NO adsorption/oxidation,[17] deoxygenation of coal bed methane on $LaCoO_3$,[18] liquid-phase organic reactions,[19] and $CaTiO_3$ nanosheets for photocatalytic hydrogen evolution.[20]

While there have been extensive computational studies of O vacancy formation energies in the bulk,[5,14,15,21] studies of surface E_{Ovac} are quite limited have been increasing

recently.[3,22−25] The band gap, bulk formation energy, and electron affinity were reported to correlate well with E_{Ovac} in d^0 and d^{10} binary oxides. Removal of neutral O results in two electrons being left behind. These electrons are excited from the valence band to the conduction band but typically relax and occupy defect states that may be lower than the conduction band minimum. Removal of O results in severing metal−O bonds, and the bulk formation energy provides a measure of the bond strength.[23] This paper reports calculated E_{Ovac} values for known perovskite structure oxides terminated by the (001) orientation. Relations between E_{Ovac} and the band gap or bulk formation energy is discussed together with strategies to reduce E_{Ovac} to obtain more reactive support materials.

2. METHODOLOGY

First-principles calculations were conducted using the projector augmented-wave method[26] and approximations as implemented in the VASP code.[27] The strongly constrained and appropriately normed (SCAN) meta generalized gradient approximation (meta-GGA)[28] was considered together with Dudarev's formulation[29] for the Hubbard U correction. The effective U value, $U − J$, which is hereafter denoted as U_{eff}, was set at 2.7 eV on the valence d states of transition metals, including lanthanides. This U_{eff} value is based on a study on
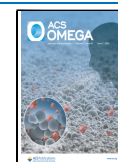
perovskite structure oxides by Wexler et al.[15] Spin-polarized calculations were conducted such that spins of an element all point in the same direction. When two cation species have nonzero spin, calculations were conducted where the spins of the two elements are parallel and antiparallel, respectively, and the lower energy spin configuration was adopted. The rationale for the selection of compounds discussed in this study is given in Supporting Information.

The surface of calculated slab models has a (001) orientation in the cubic setting. Calculations of defects, namely O vacancies, were conducted using a slab with $2\sqrt{2} \times 2\sqrt{2} \times 5$ (=40) perovskite units separated by 15 Å vacuum (the
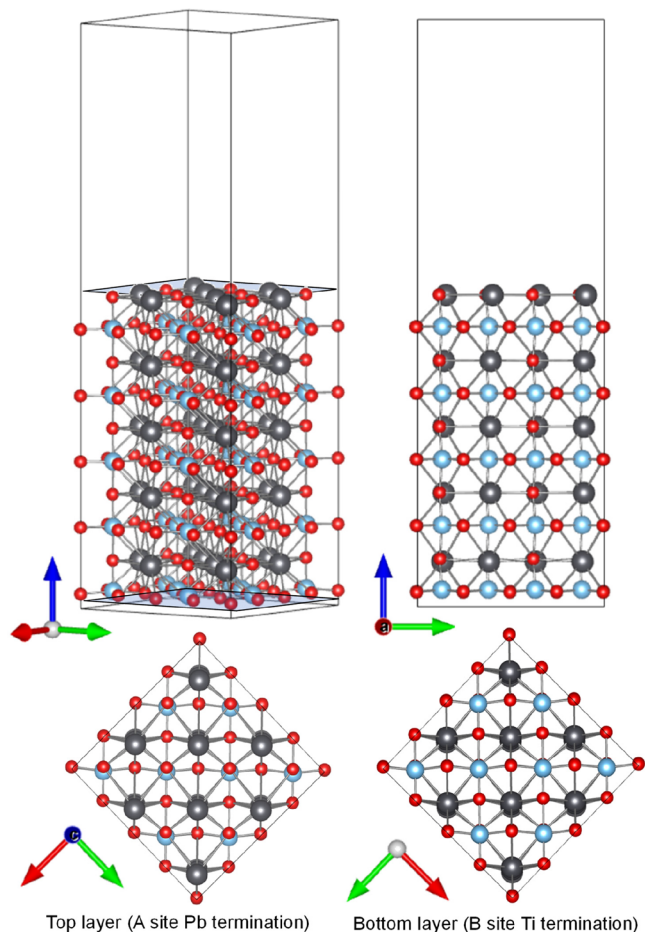

Figure 1. 200-atom slab of $PbTiO_3$. Black, blue, and red balls represent Pb, Ti, and O atoms, respectively.

PbTiO$_3$ slab is shown as an example in Figure 1). The cleavage energy is defined as

$$E_{cleave} = (E_{slab} - E_{bulk})/2A$$

where E_{slab} is the energy of the slab and E_{bulk} is that of the slab constituents when they are in a perfect bulk, respectively. Here, A is the in-plane area of the slab (blue parallelograms in Figure 1; the coefficient 2 accounts for both sides of the slab), and E_{bulk} is obtained from a bulk calculation. The surface energy of one surface is not available because a strictly nonpolar slab that is stoichiometric and where all A-cation and B-cation layers are intact cannot be obtained. The nonexistence of a nonpolar slab means that the vacuum level is ill-defined, and thus the

ionization potential, work function, and electron affinity cannot be calculated. The O vacancy formation energy E_{Ovac} is defined as

$$E_{Ovac} = E_{removed} - E_{slab} + E(O_2)/2$$

where $E_{removed}$ and $E(O_2)$ are the energy of the slab after removal of an O atom from one side of the slab (A-site or B-site cation terminated layer, hereafter A-cation and B-cation layer, respectively) and the energy of an O_2 gas molecule at 0 K, respectively.

3. RESULTS AND DISCUSSION

Tables 1 and 2 summarize the results of first-principles calculations in this study. The space group number is provided in parentheses. Table S2 in the Supporting Information shows the space group symbol and number side by side. The bulk properties shown (Table 1) are the volume per atom (v), minimum band gap (BG), bulk formation energy with respect to elementary metals and O_2 gas (E_{form}), and net spin per five atoms in the bulk (n_{spin}). Systems are identified where the Jahn–Teller effect is expected for transition metals in an octahedral coordination environment. Slab properties in Table 2, obtained for slab-and-vacuum model cells with 40 perovskite units, are E_{cleave}, the net spin of a slab (n_{spin_slab}), E_{Ovac}, and difference in net spin (Δn_{spin}) for O desorption from the A- and B-cation layers (denoted by A and B, respectively). Calculations where spin states far from the defect have changed significantly are removed from the table and not considered further. For example, the spin of the B-site cation on the surface without defects flipped after removal of O from the B-cation layer of $BaMnO_3$ (221) and $LaFeO_3$ (62).

Figure 2 plots the minimum E_{Ovac} value for O removal from the A-cation layer against the B-cation layer. There is a modest positive correlation with a coefficient of determination (R^2) of 0.64 for all shown points. The points can be categorized into three groups: Ti-containing compounds, which are clustered at the top right (high E_{Ovac}), metals at the bottom left (low E_{Ovac}), and other nonmetals. Among the "other nonmetals", O removal from the A-cation layer has lower energy when the B-site cation has fewer d electrons (V), while removal from the B-cation layer is favored in B-site cations with more d electrons (Co and Fe).

Figures S2–S4 show the partial electronic density of states (DOS) for bulk perovskites. The conduction band (CB) bottom is the B-site cation 3d states in all cases, which means that the defect state arising from electrons left in the slab after neutral O removal consists of mostly B-site cation 3d states. The nominal charge of Ti in titanates is 4+, with no 3d electrons. Notable charge states are the intermediate spin of Co^{4+} in metallic $CaCoO_3$ (62), with four spin-up electrons and one spin-down 3d electron and high-spin Mn^{3+} (d^5) and V^{4+} (d^1) in $MnVO_3$ (62).

The spin states of B-site cations in "other nonmetals" are d^1 in V^{4+} ($MnVO_3$ and $CdVO_3$), high-spin d^4 in Mn^{3+} ($BiMnO_3$), high-spin d^5 in Fe^{3+} ($LaFeO_3$), and low (no)-spin d^6 in $ScCoO_3$. Removal of O from the A-cation layer results in severing of one O–"B-cation" bond from a 6-fold coordinated B-cation, and removal from the B-cation layer causes severing of two O–"B-cation" bonds from two 5-fold-coordinated B-cations. O removal causes changes in the number of d electrons in B-cation(s), which is accompanied by a change in of the bonding environment, especially a change in the distribution of bond lengths. Removal of O from the B-cation

Table 1. Bulk Properties of Systems Considered for Defect Calculations[a]

system	v (Å³)	BG (eV)	E_{form} (eV/atom)	n_{spin} (elementary charge/5 atoms)
BaFeO₃ (221)	12.50	0.02	−2.31	4.19
BaFeO₃ (123)	12.50	0.02	−2.31	4.19
BaMnO₃ (221)	12.27	0.00	−5.84	3.25
BaTiO₃ (221)	12.97	2.46	−3.58	0.00
BaTiO₃ (123)	12.97	2.46	−3.58	0.00
BaTiO₃ (99)	12.98	2.46	−3.58	0.00
BaTiO₃ (38)	12.97	2.45	−3.58	0.00
BaVO₃ (221)	12.42	0.01	−3.02	1.00
BiMnO₃ (62)	12.09	0.65	−5.11	4.00
BiMnO₃ (15)	12.42	0.57	−5.11	4.00
CaCoO₃ (62)	10.58	0.01	−2.09	3.00
CaTiO₃ (62)	11.30	3.24	−3.65	0.00
CdTiO₃ (62)	11.08	3.06	−2.75	0.00
CdTiO₃ (33)	11.07	3.06	−2.75	0.00
CdVO₃ (62)	10.74	1.04	−2.28	1.00
ScCoO₃ (62)	9.43	2.41	−2.72	0.00
LaFeO₃ (62)	12.25	1.07	−3.09	5.00
SrFeO₃ (221)	11.34	0.01	−2.42	4.01
SrFeO₃ (123)	11.34	0.01	−2.42	4.01
MnTiO₃ (62)	10.46	2.13	−6.52	5.00
MnVO₃ (62)	10.11	0.38	−6.06	6.00
PbTiO₃ (99)	12.56	2.37	−2.68	0.00
SrTiO₃ (221)	12.10	2.62	−3.65	0.00
SrTiO₃ (140)	12.08	2.69	−3.65	0.00
SrVO₃ (221)	11.49	0.02	−3.11	1.00
YTiO₃ (62)	12.00	1.85	−3.79	1.00

[a]The parentheses following the compound name indicate the space group number.

Table 2. Bulk Properties of Systems Considered for Defect Calculations[a]

system	E_{cleave} (eV/Å³)	n_{spin_slab} (elementary charge/200 atoms)	E_{Ovac} (A, eV)	E_{Ovac} (B, eV)	Δn_{spin} (A, elementary charge/defect)	Δn_{spin} (B, elementary charge/defect)
BaFeO₃ (221)	47.99	170.42	0.92	−0.40	7.75	6.22
BaFeO₃ (123)	49.80	170.64	0.60	−1.14	7.85	3.53
BaMnO₃ (221)	41.60	78.35				
BaTiO₃ (221)	60.19	0.00	5.53	4.72	0.90	1.18
BaTiO₃ (123)	60.27	0.00	5.54	4.61	0.89	2.00
BaTiO₃ (99)	61.39	0.00	5.53	4.30	0.45	1.01
BaTiO₃ (38)	60.64	0.00	5.53	4.39	1.55	1.00
BaVO₃ (221)	20.69	40.00				
BiMnO₃ (62)	22.85	160.00	1.94	2.12	2.02	2.02
BiMnO₃ (15)	35.05	159.97	3.08	2.50	0.00	2.00
CaCoO₃ (62)	52.35	100.01	0.02		4.01	
CaTiO₃ (62)	73.56	0.00	5.78	5.74	0.00	1.02
CdTiO₃ (62)	72.81	0.00	3.17	4.56	0.00	0.72
CdTiO₃ (33)	72.77	0.00	3.17	4.25	0.00	2.00
CdVO₃ (62)	68.32	40.00	0.88	2.39	2.00	2.00
ScCoO₃ (62)	105.40	3.63	3.70	0.79	3.63	1.63
LaFeO₃ (62)	88.68	197.53	5.01		3.95	
SrFeO₃ (221)	59.89	164.68	1.19	0.10	2.27	0.64
SrFeO₃ (123)	60.24	164.56	0.95	−0.22	1.98	0.67
MnTiO₃ (62)	75.31	200.00	4.48	5.70	0.00	0.24
MnVO₃ (62)	69.58	240.00	1.35	2.50	2.00	2.00
PbTiO₃ (99)	47.01	0.00	4.31	4.40	0.00	2.00
SrTiO₃ (221)	69.63	0.00	5.58	4.81	1.20	2.00
SrTiO₃ (140)	69.38	0.00	5.62	5.27	1.28	1.02
SrVO₃ (221)	43.23	40.00				
YTiO₃ (62)	100.95	40.00	4.98	4.64	0.00	2.00

[a]The parentheses following the compound name indicate the space group number. A and B represent O removal from the A-cation and B-cation layer, respectively.
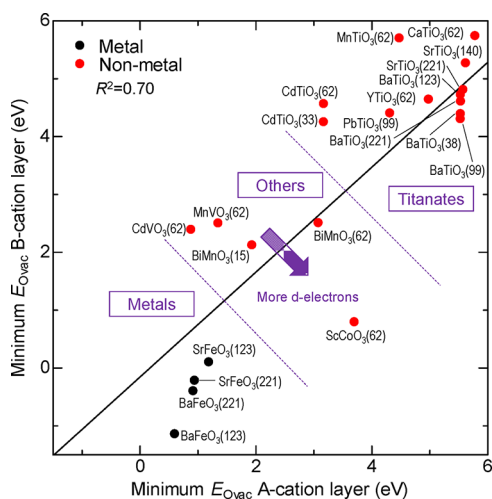
Figure 2. Plot of minimum E_{Ovac} values for A- against B-cation layers.

layer results in a higher flexibility because a bond is severed from B-cations with already missing bonds. This could be the reason for the smaller spread in E_{Ovac} values for O removal from the B-cation layer in comparison to the A-cation layer for "other nonmetals" in Figure 2. In particular, Fe–O and Co–O bond lengths in $LaFeO_3$ (62) and $ScCoO_3$ (62) are almost all the same. Adding extra electrons from O removal from the A-cation layer forces Jahn–Teller distortion to the Fe or Co that bonded to the removed O, which would force large local changes in bond lengths and/or unfavorable electronic states in Fe or Co. The lack of mitigating mechanisms could lead to the high E_{Ovac} values for O removal from the A-cation layer in $LaFeO_3$ (62) and $ScCoO_3$ (62).

Figure 3 gives a plot of BG versus minimum E_{Ovac}. The space group number is shown together with the chemical formula.
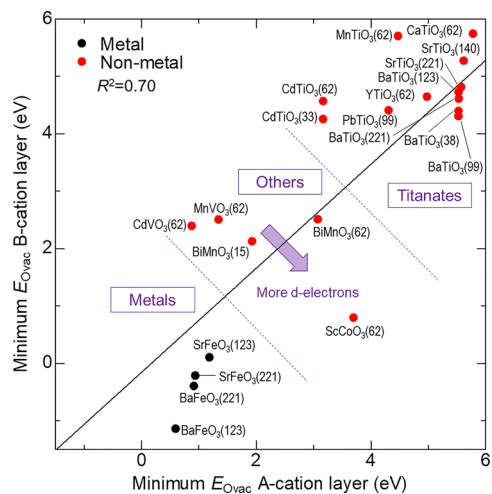

Figure 3. BG versus E_{Ovac} for O removal from (a) A- and (b) B-cation layers.

There is a positive correlation trend in both the A- and B-site terminated layers, with the lowest E_{Ovac} value being found in metallic systems. This trend was also found in binary carbide, nitride,[24] and d^0 and d^{10} binary oxide systems,[23] but not in zinc-containing normal spinels.[25] On the other hand, Figure 4 shows plots of E_{form} versus minimum E_{Ovac}. A negative correlation is found, which is consistent with d^0 and d^{10} binary
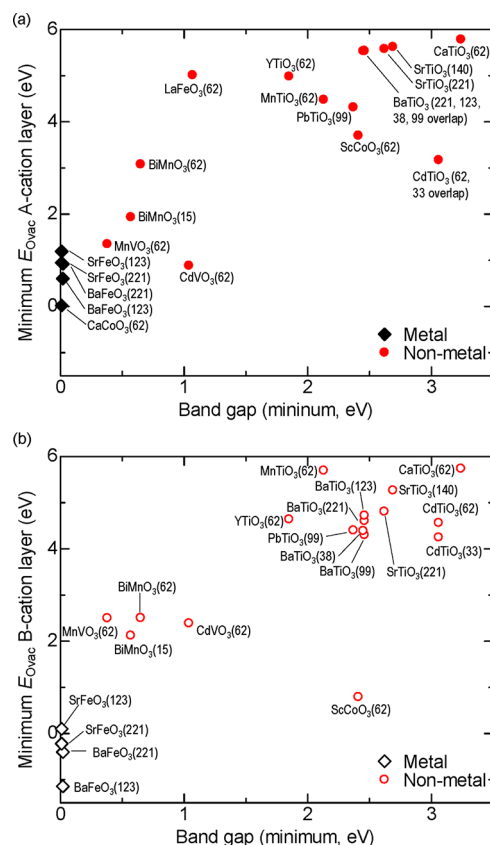

Figure 4. E_{form} versus E_{Ovac} for O removal from (a, top) A- and (b, bottom) B-cation layers.

oxide systems[23] as well as the (100) and (110) surfaces of Zn-containing normal spinels.[25] E_{Ovac} from the B-cation layer of $ScCoO_3$ (62) appears to be an extreme layer for the BG plot (Figure 3b) but is not in the E_{form} plot (Figure 4b). The high E_{Ovac} in titanates comes from the electronic structure; all titanates have BG values exceeding 1.5 eV, and all nontitanates except for $ScCoO_3$ have BG values below 1.5 eV (Figure 4).

Figure 5 shows the DOS of the bulk, slab, and slab with O removed from the A- and B-cation layers of $CdTiO_3$ (33) and $ScCoO_3$ (62). The formation of surfaces results in the formation of surface states within the band gap. The formation of O vacancies results in additional defect states. In $CdTiO_3$ (33) (Figure 5(a,c,e,f)), the defect state is closer to the valence band in O removal from the A-cation layer in comparison to that from the B-cation layer, and this is reflected in the lower E_{Ovac} in the former. On the other hand, the Fermi level after O removal is at the top of the valence band in $ScCoO_3$ (62) (Figure 5(b,d,f,h)). Variations in the defect state position among various compounds was also observed in d^0 and d^{10} binary oxides.[23]

4. SUMMARY

We calculated the E_{Ovac} values for perovskite-structure oxides with a transition metal (Ti–Fe) as the B-site cation. The E_{Ovac} correlates well with the band gap and bulk formation energy, which is a trend also found in other oxides. A low E_{Ovac} value, which is expected to result in higher catalytic activity, is found in metallic perovskites such as $CaCoO_3$, $BaFeO_3$, and $SrFeO_3$. On the other hand, titanates had high E_{Ovac} values, typically exceeding 4 eV/atom.
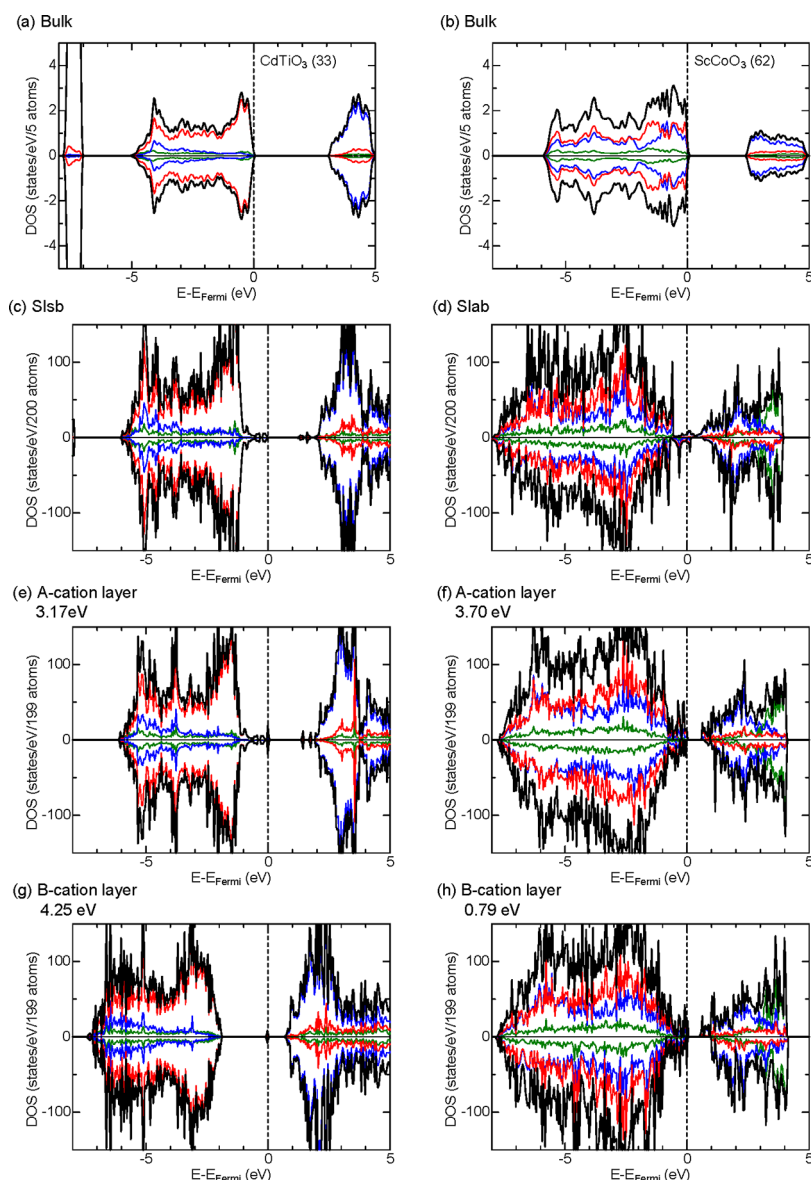
Figure 5. DOS of (a, b) bulk, (c, d) slab, and slabs with O removed from the (e, f) A- and (g, h) B-cation layers of (a, c, e, f) CdTiO$_3$ (space group number 33) and (b, d, f, h) ScCoO$_3$ (62). The E_{Ovac} value is also shown.

■ ASSOCIATED CONTENT

Ⓢ Supporting Information

The Supporting Information is available free of charge at https://pubs.acs.org/doi/10.1021/acsomega.2c00702.

> Justification of the selection of perovskite compounds considered in this study and electronic DOS of select bulk states (PDF)

■ AUTHOR INFORMATION

Corresponding Author

Yoyo Hinuma − *Department of Energy and Environment, National Institute of Advanced Industrial Science and Technology (AIST), Ikeda 563-8577, Japan;* ⓞ orcid.org/ 0000-0003-2272-1178; Email: y.hinuma@aist.go.jp

Authors

Shinya Mine − *Institute for Catalysis, Hokkaido University, Sapporo 001-0021, Japan;* ⓞ orcid.org/0000-0002-8339-0301

Takashi Toyao − *Institute for Catalysis, Hokkaido University, Sapporo 001-0021, Japan; Elements Strategy Initiative for Catalysts and Batteries, Kyoto University, Kyoto 615-8520, Japan;* ⓞ orcid.org/0000-0002-6062-5622

Ken-ichi Shimizu − *Institute for Catalysis, Hokkaido University, Sapporo 001-0021, Japan; Elements Strategy Initiative for Catalysts and Batteries, Kyoto University, Kyoto 615-8520, Japan;* ⓞ orcid.org/0000-0003-0501-0294

Complete contact information is available at:
https://pubs.acs.org/10.1021/acsomega.2c00702

Notes

The authors declare no competing financial interest.

■ ACKNOWLEDGMENTS

University, the Joint Usage/Research Center for Catalysis at Hokkaido University, and the Supercomputer Center in the Institute for Solid State Physics at the University of Tokyo were used. The VESTA code[30] was used to draw Figure 1, and Figure S1.

■ REFERENCES

(1) Pacchioni, G. Oxygen Vacancy: The invisible agent on oxide surfaces. *ChemPhysChem* **2003**, *4*, 1041−1047. Oba, F.; Choi, M.; Togo, A.; Tanaka, I. Point defects in ZnO: An approach from first principles. *Sci. Technol. Adv. Mater.* **2011**, *12*, 034302−034302. Rousseau, R.; Glezakou, V.-A.; Selloni, A. Theoretical insights into the surface physics and chemistry of redox-active oxides. *Nature Reviews Materials* **2020**, *5* (6), 460−475.

(2) Ganduglia-Pirovano, M. V.; Hofmann, A.; Sauer, J. Oxygen vacancies in transition metal and rare earth oxides: Current state of understanding and remaining challenges. *Surf. Sci. Rep.* **2007**, *62* (6), 219−270.

(3) Daelman, N.; Hegner, F. S.; Rellán-Piñeiro, M.; Capdevila-Cortada, M.; García-Muelas, R.; López, N. Quasi-degenerate states and their dynamics in oxygen deficient reducible metal oxides. *J. Chem. Phys.* **2020**, *152* (5), 050901.

(4) Linderälv, C.; Lindman, A.; Erhart, P. A unifying perspective on oxygen vacancies in wide band gap oxides. *J. Phys. Chem. Lett.* **2018**, *9*, 222−228.

(5) Emery, A. A.; Saal, J. E.; Kirklin, S.; Hegde, V. I.; Wolverton, C. High-throughput computational screening of Pperovskites for thermochemical water splitting applications. *Chem. Mater.* **2016**, *28* (16), 5621−5634.

(6) Park, J. S.; Kim, S.; Xie, Z.; Walsh, A. Point defect engineering in thin-film solar cells. *Nature Reviews Materials* **2018**, *3* (7), 194−210. Freysoldt, C.; Grabowski, B.; Hickel, T.; Neugebauer, J.; Kresse, G.; Janotti, A.; Van De Walle, C. G. First-principles calculations for point defects in solids. *Rev. Mod. Phys.* **2014**, *86*, 253−305. Yu, X.; Marks, T. J.; Facchetti, A. Metal oxides for optoelectronic applications. *Nat. Mater.* **2016**, *15* (4), 383−396.

(7) Setvín, M.; Wagner, M.; Schmid, M.; Parkinson, G. S.; Diebold, U. Surface point defects on bulk oxides: Atomically-resolved scanning probe microscopy. *Chem. Soc. Rev.* **2017**, *46*, 1772−1784.

(8) Kumar, G.; Lau, S. L. J.; Krcha, M. D.; Janik, M. J. Correlation of methane activation and oxide catalyst reducibility and its implications for oxidative coupling. *ACS Catal.* **2016**, *6* (3), 1812−1821.

(9) Yang, C.; Yu, X.; Heißler, S.; Weidler, P. G.; Nefedov, A.; Wang, Y.; Wöll, C.; Kropp, T.; Paier, J.; Sauer, J. O₂ activation on ceria catalysts—the importance of substrate crystallographic orientation. *Angewandte Chemie - International Edition* **2017**, *56*, 16399−16404. Agarwal, S.; Zhu, X.; Hensen, E. J. M.; Lefferts, L.; Mojet, B. L. Defect chemistry of ceria nanorods. *J. Phys. Chem.C* **2014**, *118*, 4131−4142. Zhang, Z.; Bondarchuk, O.; White, J. M.; Kay, B. D.; Dohnálek, Z. Imaging adsorbate O−H bond cleavage: methanol on TiO₂(110). *J. Am. Chem. Soc.* **2006**, *128* (13), 4198−4199. Tong, X.; Benz, L.; Chrétien, S.; Metiu, H.; Bowers, M. T.; Buratto, S. K. Direct visualization of water-induced relocation of Au atoms from oxygen vacancies on a TiO₂(110) surface. *J. Phys. Chem. C* **2010**, *114* (9), 3987−3990. Pacchioni, G.; Freund, H. *Electron transfer at oxide surfaces. the MgO paradigm: From defects to ultrathin films* **2013**, *113*, 4035−4072. Setvín, M.; Wagner, M.; Schmid, M.; Parkinson, G. S.; Diebold, U. Surface point defects on bulk oxides: atomically-resolved scanning probe microscopy. *Chem. Soc. Rev.* **2017**, *46* (7), 1772−1784.

(10) Zhang, D.; Han, Z.-K.; Murgida, G. E.; Ganduglia-Pirovano, M. V.; Gao, Y. Oxygen-vacancy dynamics and entanglement with polaron hopping at the reduced CeO₂ (111) surface. *Phys. Rev. Lett.* **2019**, *122* (9), 096101. Han, Z.-K.; Zhang, L.; Liu, M.; Ganduglia-Pirovano, M. V.; Gao, Y. The structure of oxygen vacancies in the near-surface of reduced CeO₂ (111) under strain. *Frontiers in Chemistry* **2019**, *7*, 1.

(11) Reticcioli, M.; Setvin, M.; Hao, X.; Flauger, P.; Kresse, G.; Schmid, M.; Diebold, U.; Franchini, C. Polaron-driven surface reconstructions. *Physical Review X* **2017**, *7* (3), 031053.

(12) Honkala, K. Tailoring oxide properties: An impact on adsorption characteristics of molecules and metals. *Surf. Sci. Rep.* **2014**, *69*, 366−388.

(13) Haubrich, J.; Kaxiras, E.; Friend, C. M. The role of surface and subsurface point defects for chemical model studies on TiO₂: A first-principles theoretical study of formaldehyde bonding on rutile TiO₂(110). *Chem. - Eur. J.* **2011**, *17*, 4496−4506. Yin, W.-J.; Wei, S.-H.; Al-Jassim, M. M.; Yan, Y. Prediction of the chemical trends of oxygen vacancy levels in binary metal oxides. *Appl. Phys. Lett.* **2011**, *99* (14), 142109. Albuquerque, A. R.; Bruix, A.; Dos Santos, I. M. G.; Sambrano, J. R.; Illas, F. DFT study on Ce-doped anatase TiO₂: Nature of Ce³⁺ and Ti³⁺ centers triggered by oxygen vacancy formation. *J. Phys. Chem. C* **2014**, *118*, 9677−9689. Gerosa, M.; Bottani, C. E.; Caramella, L.; Onida, G.; Di Valentin, C.; Pacchioni, G. Defect calculations in semiconductors through a dielectric-dependent hybrid DFT functional: The case of oxygen vacancies in metal oxides. *J. Chem. Phys.* **2015**, *143*, 134702−134702. Dickens, C. F.; Nørskov, J. K. A theoretical investigation into the role of surface defects for oxygen evolution on RuO₂. *J. Phys. Chem. C* **2017**, *121*, 18516−18524. Grimaud, A.; Diaz-Morales, O.; Han, B.; Hong, W. T.; Lee, Y.-L.; Giordano, L.; Stoerzinger, K. A.; Koper, M. T. M.; Shao-Horn, Y. Activating lattice oxygen redox reactions in metal oxides to catalyse oxygen evolution. *Nat. Chem.* **2017**, *9* (5), 457−465. Rellán-Piñeiro, M.; López, N. One oxygen vacancy, two charge states: characterization of reduced α-MoO₃ (010) through theoretical methods. *J. Phys. Chem. Lett.* **2018**, *9*, 2568−2573.

(14) Curnan, M. T.; Kitchin, J. R. Effects of concentration, crystal structure, magnetism, and electronic structure method on first-principles oxygen vacancy formation energy trends in perovskites. *J. Phys. Chem. C* **2014**, *118* (49), 28776−28790.

(15) Wexler, R. B.; Gautam, G. S.; Stechel, E. B.; Carter, E. A. Factors governing oxygen vacancy formation in oxide perovskites. *J. Am. Chem. Soc.* **2021**, *143* (33), 13212−13227.

(16) Saito, H.; Seki, H.; Hosono, Y.; Higo, T.; Seo, J. G.; Maeda, S.; Hashimoto, K.; Ogo, S.; Sekine, Y. Dehydrogenation of ethane via the Mars−van Krevelen Mmechanism over La₀.₈Ba₀.₂MnO₃₋δ perovskites under anaerobic conditions. *J. Phys. Chem. C* **2019**, *123* (43), 26272−26281.

(17) Hwang, J.; Rao, R. R.; Giordano, L.; Akkiraju, K.; Wang, X. R.; Crumlin, E. J.; Bluhm, H.; Shao-Horn, Y. Regulating oxygen activity of perovskites to promote NOx oxidation and reduction kinetics. *Nature Catalysis* **2021**, *4* (8), 663−673. Onrubia-Calvo, J. A.; Pereda-Ayo, B.; González-Velasco, J. R. Perovskite-based catalysts as efficient, durable, and economical NOx storage and reduction systems. *Catalysts* **2020**, *10* (2), 208.

(18) Zhao, Z.; Wang, L.; Ma, J.; Feng, Y.; Cao, X.; Zhan, W.; Guo, Y.; Guo, Y.; Lu, G. Deoxygenation of coal bed methane on LaCoO₃ perovskite catalyst: the structure evolution and catalytic performance. *RSC Adv.* **2017**, *7* (25), 15211−15221.

(19) Kamata, K. Perovskite oxide catalysts for liquid-phase organic reactions. *Bull. Chem. Soc. Jpn.* **2019**, *92* (1), 133−151.

(20) Cai, J.; Cao, A.; Huang, J.; Jin, W.; Zhang, J.; Jiang, Z.; Li, X. Understanding oxygen vacancies in disorder-engineered surface and Ssubsurface of CaTiO₃ nanosheets on photocatalytic hydrogen evolution. *Appl. Catalysis B: Environmental* **2020**, *267*, 118378.

(21) Deml, A. M.; Stevanović, V.; Muhich, C. L.; Musgrave, C. B.; O'Hayre, R. Oxide enthalpy of formation and band gap energy as accurate descriptors of oxygen vacancy formation energetics. *Energy Environ. Sci.* **2014**, *7* (6), 1996−2004. Deml, A. M.; Holder, A. M.; O'Hayre, R. P.; Musgrave, C. B.; Stevanović, V. Intrinsic material properties dictating oxygen vacancy formation energetics in metal oxides. *J. Phys. Chem. Lett.* **2015**, *6* (10), 1948−1953. Mishra, A.; Li, T.; Li, F.; Santiso, E. E. Oxygen vacancy creation energy in Mn-containing perovskites: An effective indicator for chemical looping with oxygen uncoupling. *Chem. Mater.* **2019**, *31* (3), 689−698. Lee, H.; Gwon, O.; Choi, K.; Zhang, L.; Zhou, J.; Park, J.; Yoo, J.-W.;

Wang, J.-Q.; Lee, J. H.; Kim, G. Enhancing bifunctional electrocatalytic activities via metal d-band center lift induced by oxygen vacancy on the subsurface of perovskites. *ACS Catal.* **2020**, *10* (8), 4664−4670.

(22) Yoo, J. S.; Rong, X.; Liu, Y.; Kolpak, A. M. Role of lattice oxygen participation in understanding trends in the oxygen evolution reaction on perovskites. *ACS Catal.* **2018**, *8* (5), 4628−4636. Su, H.-Y.; Ma, X.; Sun, K.; Sun, C.; Xu, Y.; Calle-Vallejo, F. Trends in C−O and N−O bond scission on rutile oxides described using oxygen vacancy formation energies. *Chemical Science* **2020**, *11* (16), 4119−4124.

(23) Hinuma, Y.; Toyao, T.; Kamachi, T.; Maeno, Z.; Takakusagi, S.; Furukawa, S.; Takigawa, I.; Shimizu, K. Density functional theory calculations of oxygen vacancy formation and subsequent molecular adsorption on oxide surfaces. *J. Phys. Chem. C* **2018**, *122* (51), 29435−29444.

(24) Hinuma, Y.; Mine, S.; Toyao, T.; Maeno, Z.; Shimizu, K. Surface activation by electron scavenger metal nanorod adsorption on TiH_2, TiC, TiN, and Ti_2O_3. *Phys. Chem. Chem. Phys.* **2021**, *23* (31), 16577−16593.

(25) Hinuma, Y.; Mine, S.; Toyao, T.; Kamachi, T.; Shimizu, K.. Factors determining surface oxygen vacancy formation energy in Ternary spinel structure oxides with zinc. *Phys. Chem. Chem. Phys.* **2021**, *23* (41), 23768−23777.

(26) Blöchl, P. E. Projector augmented-wave method. *Phys. Rev. B* **1994**, *50* (24), 17953−17979.

(27) Kresse, G.; Furthmüller, J. Efficient iterative schemes for ab initio total-energy calculations using a plane-wave basis set. *Phys. Rev. B* **1996**, *54* (16), 11169−11186. Kresse, G.; Joubert, D. From ultrasoft pseudopotentials to the projector augmented-wave method. *Phys. Rev. B* **1999**, *59* (3), 1758−1775.

(28) Sun, J.; Ruzsinszky, A.; Perdew, J. P. Strongly constrained and appropriately normed semilocal density functional. *Phys. Rev. Lett.* **2015**, *115* (3), 036402.

(29) Dudarev, S. L.; Botton, G. A.; Savrasov, S. Y.; Humphreys, C. J.; Sutton, A. P. Electron-energy-loss spectra and the structural stability of nickel oxide: An LSDA+U Study. *Phys. Rev. B* **1998**, *57* (3), 1505−1509.

(30) Momma, K.; Izumi, F. VESTA 3 for three-dimensional visualization of crystal, volumetric and morphology data. *J. Appl. Crystallogr.* **2011**, *44* (6), 1272−1276.